PCCP

ROYAL SOCIETY OF CHEMISTRY

PAPER

View Article Online
View Journal



Cite this: DOI: 10.1039/d6cp01088a

# Water interactions with condensed carboxylic acids: adsorption and desorption of water on valeric acid surfaces

Sofia M. Johansson,† Josip Lovrić,‡ Erik S. Thomson, Xiangrui Kong * and Jan B. C. Pettersson *

Received 25th March 2026,
Accepted 29th April 2026

DOI: 10.1039/d6cp01088a

rsc.li/pccp

Organic aerosol particles undergo phase transitions through water uptake and release, which directly influence their physicochemical properties and impact aerosol–cloud interactions, climate, and air quality. Here, we combine environmental molecular beam (EMB) experiments with molecular dynamics (MD) simulations to investigate water interactions with valeric acid (VA) as a model organic aerosol system. Water molecules colliding with VA surfaces are predominantly trapped, with only a minor inelastic scattering channel observed. Most trapped molecules are weakly bound and desorb rapidly (69–83%), while a smaller fraction occupies more strongly bound surface states, leading to desorption on millisecond timescales (7–16%) or longer-term accommodation (5–20%). The water sticking coefficient shows little temperature dependence over 160–260 K, but depends strongly on film thickness, *i.e.*, molecularly thin VA coatings exhibit higher sticking probabilities than micrometer-thick layers. These results suggest that molecularly thin VA coatings may exhibit differences in molecular arrangement that could contribute to differences in hygroscopic behavior compared to bulk-like surfaces.



## 1. Introduction

Aerosol particles scatter and absorb solar radiation, and thereby alter the global radiative balance and influence climate.[1,2] As abundant aerosol components, organic compounds contribute significantly to new particle formation and growth of pre-existing particles.[3,4] However, the number of different organic compounds in the atmosphere is high, and there remains a lack of understanding regarding how this diversity of interacting components influences aerosol properties, clouds, and climate feedbacks. Such knowledge gaps contribute to climate model and prediction uncertainties in many fundamental ways.[5,6]

Carboxylic acids are one of the most common reaction products from oxidation of volatile organic compounds (VOCs).[7,8] Small carboxylic acids are highly water-soluble and hygroscopic, and are therefore ubiquitous in aqueous aerosol particles. This makes them active participants in aerosol–cloud interactions, influencing hygroscopic growth and cloud droplet activation.[9–11] High relative humidity (RH) has been confirmed to favor formation of secondary inorganic aerosol (SIA), which strongly relates to haze episodes in urban areas.[12,13] The effects of RH on secondary organic aerosol (SOA) are, however, more complicated. Here water influences the interplay of multiple factors such as photochemistry, particle acidity, viscosity and phase state.[10] At atmospheric conditions organic aerosols exist in a wide range of different states, like amorphous glassy solids, highly viscous semi-solids and liquids.[14] By adsorbing and/or desorbing water from the surroundings, organic aerosol particles may transition between states,[15,16] and these processes will in turn have direct feedbacks on the particles' chemical and physical characteristics. Thus, in addition to providing fundamental insight, understanding mechanisms of water uptake by atmospheric organics affects our ability to resolve and model aerosol particles and the complex climate system. In the present work, valeric acid surfaces are used as well-defined model systems to probe elementary gas-surface interaction processes such as trapping, desorption, and accommodation. While such condensed surfaces are not direct analogues of liquid aerosol droplets, the interfacial region in both systems involves confined or partially coordinated water molecules. Studying these interactions therefore provides molecular-level insight into processes that are relevant for water uptake at organic aerosol interfaces.

Several short-chained carboxylic acids present in the atmosphere have been studied using molecular dynamics (MD) simulations focused on interactions with water at molecular

*Department of Chemistry and Molecular Biology, University of Gothenburg, 413 90 Gothenburg, Sweden. E-mail: kongx@chem.gu.se, janp@chem.gu.se*
† Now at: Renova AB, 401 22 Gothenburg, Sweden.
‡ Now at: AstraZeneca, 431 83 Mölndal, Sweden.

levels.[17–23] For example, the mixing state of formic acid and water is driven by the water content and temperature; where at cold and dry conditions water forms islands on top of the formic acid aggregate surface, and in contrast at warm conditions and high RH the mixing is more homogeneous.[18] Similar behavior has been reported for other short-chain carboxylic acids, such as acetic and propionic acid, where hydrogen bonding and interfacial structuring govern water uptake and mixing.[19,21,23] Recently, water on valeric acid (VA) was reported to form small water islands on the surface of VA aggregates at low RH, and to partially penetrate into the bulk, while at high RH the majority of the water remains on the surface.[20] The VA is a product of fermentation and/or chemical transformation of lignocellulosic feedstocks, thus it is a common gas molecule during biomass energy conversion processes. These studies provide insight into water-carboxylic acid interaction motifs at the molecular level. In the present work, the solid VA surfaces are treated as simplified model interfaces and are not intended to directly represent the structure of atmospheric aggregates.

There is also considerable fundamental interest in the surface properties of organic compounds. The VA crystal structure deviates from those of other linear carboxylic acids.[24] While carboxylic acids mostly form bilayer crystal structures, VA exhibits a zig-zag pattern inside the monolayer. Evidently, this induces a different surface organization compared to other carboxylic acids. In addition, many crystals undergo surface changes in terms of increased disorder and/or melting below the bulk melting point,[25,26] but the importance of these processes for organic crystals and the associated effects on gas uptake is incompletely understood.

In this study, we focus on the water interactions with VA surfaces, by employing the environmental molecular beam (EMB) method,[27,28] while conducting complementary MD simulations as investigative tools. The EMB technique has been used for detailed studies of dynamics and kinetics of gas–surface interactions, including several water-organics systems,[29–35] water-bare ice[36] and water-organic coated ice,[37] water-graphite,[38] as well as organic-graphite[39] and organic–organic systems.[40,41] The information from the EMB and MD methods are complementary and thus these methods have been combined beneficially in several recent studies.[34,35,39,42] Here, they are used to investigate the water uptake and sorption kinetics and dynamics in a water-VA interfacial system.

## 2. Methodology

### 2.1. Environmental molecular beam experiments

The EMB experimental method is used to illuminate the detailed interactions between water and VA surfaces. Here a brief description of the technique is provided, with a more detailed description available in a previously published paper.[27] The EMB apparatus including its main components are schematically presented in Fig. 1a. The beam is introduced into a differentially pumped multi-chambered vacuum system through a pulsed gas source. A well-defined low-density beam is formed by selecting molecules using an inverted cone (*i.e.* a skimmer), and a rotating chopper with a fixed-frequency (120 Hz) that defines the pulse length. The beam consists of a mixture of He and $D_2O$ with a total pressure of $1.2 \times 10^5$ Pa and a partial $D_2O$ pressure of $2.3 \times 10^3$ Pa, equal to approximately $10^{11}$ $D_2O$ molecules per pulse. The average kinetic energy of $D_2O$ molecules is $22.5 \pm 0.5$ kJ mol$^{-1}$. Deuterium oxide ($D_2O$ 99.9%, Sigma-Aldrich Co.) is used to differentiate beam molecules from $H_2O$ in the background gas, thus enhancing the signal-to-noise ratio. The molecular beam (MB) travels through high vacuum until it enters an environmental chamber through a grated opening that separates high and low-vacuum regions (Fig. 1b and c). Within the environmental chamber a $5 \times 6$ mm$^2$ graphite substrate (highly oriented pyrolytic graphite, grade ZYB, Advanced Ceramics Corp.) is situated 1.6 mm behind the grating. The substrate temperature is controlled by simultaneous liquid nitrogen cooling and PID-controlled resistive heating, enabling stable temperatures in the range 160–260 K, which is relevant for cold atmospheric conditions such as upper tropospheric and polar environments. The beam collides with the surface with an incident angle of 45° with respect to the surface normal. Thus molecules that scatter in the specular direction travel a 4.4 mm distance within the low-vacuum region before exiting the environmental chamber. Valeric acid vapor is introduced into the low-vacuum environmental chamber through a gas inlet regulated by a leak valve. The molecular flux leaving the environmental chamber is detected using a rotatable quadrupole mass spectrometer (QMS).

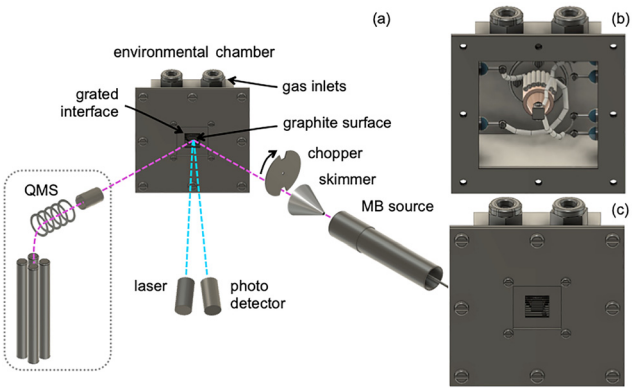


Fig. 1 (a) A schematic view of the EMB apparatus. The molecular beam and laser are shown as pink and blue dashed lines, respectively. To the right, a zoomed-in view of the (b) open and (c) enclosed environmental chamber with a grated opening.

During experiments, VA condensation and evaporation processes on the graphite substrate are monitored using helium and light (670 nm) scattering. Elastic scattering of helium is highly sensitive to initial surface coverage, while the light scattering provides information about layer thickness and morphology for thicker adsorbates. Once a VA layer coats the graphite substrate the leak valve can be adjusted to maintain steady state conditions throughout the measurements. From

160 K to 220 K, thick solid VA layers ($\approx$ 1 μm thickness) can be stably adsorbed and maintained. At temperatures above $\sim$220 K, these thick layers become unstable under the experimental conditions, whereas molecularly thin VA coatings on graphite remain stable and can therefore be examined at higher temperatures. The latter is too thin to be observed with the optical method, but is detected by helium scattering. This suggests that a condensed phase consisting of one or a few molecular layers has properties that make it more stable than bulk VA. The bulk melting temperature $T_m$ of solid VA is 239.6 K, suggesting that the thicker layers form a solid coating.[43] During measurements the MB is directed onto the VA coated substrate and the QMS detects the outgoing molecular flux for 10 ms time windows after each beam pulse impacts the surface. Given that the beam source-to-surface and surface-to-detector distances are well known the resulting data takes the form of mass intensity as a function of arrival time or equivalently reformulated as Time-of-Flight (ToF) distributions. Between measurements the graphite substrate is cleaned by increasing its temperature to 600 K, typically for a period of $>$12 hours.

### 2.2. Analysis of EMB data

The EMB method directly follows the fate of the beam molecules after colliding with the surface, which due to the experimental setup may include scattering and thermal desorption. Impinging molecules can thermalize and form bonds of various binding energies with the surfaces. Subsequently the desorption flux may consist of multiple desorption components with different rates,[34] and kinetic models may be required to interpret individual components based on the experimental results.[36]

The ToF distributions generated during experiments are analyzed to gain information about the kinetics and dynamics of the interactions between water molecules in the beam and the condensed VA layers. The time-dependent water flux from the surface may be explained as a combination of three components: a fast component related to inelastic scattering (IS) and two thermal desorption (TD) components with significantly different rate coefficients. In the analysis procedure, a non-linear, least-squares minimization is used to identify the optimum convolution of the incident beam profile, the IS component, and the TD components that best represent the ToF data. In these VA studies it becomes obvious that one IS and one TD channel cannot sufficiently fit the experimental data, whereas two desorption components adequately explain the ToF data. The inelastic component may be described as a modified Maxwell–Boltzmann distribution,[44]

$$I_{IS}(v(t)) = C_i v(t)^4 \exp\left[-\left(\frac{v(t)-\bar{v}}{\sqrt{\frac{2k_B T_{IS}}{m}}}\right)^2\right], \quad (1)$$

where $C_i$ is a free fitted scaling parameter which sets the magnitude of the IS component, $v$ is the velocity of the molecules, $\bar{v}$ is a free fitting parameter representing the average IS velocity, $k_B$ is the Boltzmann constant, $m$ is the mass of the $D_2O$ molecule, and $T_{IS}$ is a free fitting parameter indicative of the velocity spread of the IS component. Here, $T_{IS}$ is an effective fitting parameter describing the velocity spread of the inelastically scattered molecules and does not represent the physical surface temperature, since these molecules have not fully equilibrated with the surface.

Molecules that are thermalized in the interactions with the surface spend a finite time on the surface before desorbing. Thermal desorption is best explained as a convolution of two distributions, one $I_{TDa}$ that relates desorption velocities to the surface temperature,

$$I_{TDa}(v(t)) = C_j v(t)^4 \exp\left[-\left(\frac{v(t)}{\sqrt{\frac{2k_B T_s}{m}}}\right)^2\right], \quad (2)$$

where $C_j$ is a free scaling factor, $T_s$ is the surface temperature and the other variables remain as in eqn (1). The second distribution $I_{TDb}$ describes the exponential decay of the TD component by relating desorption to the surface residence time of water molecules,

$$I_{TDb} = C_j e^{-kt}. \quad (3)$$

Here the desorption rate coefficient $k$ serves as a fitting parameter, $t$ is the molecular arrival time, and due to the convolution $C_j$ is a degenerate scaling factor with that given in eqn (2).

Hence, the fits of experimental ToF distributions are carried out with 7 free parameters. These parameters are also restricted by the physics of the components that they are describing, which limits the flexibility of solutions. Nevertheless, the most sensitive part is the IS component, due to its low intensity and relatively high noise in the beginning of ToFs, which makes the fittings slightly vary depending on the initial guess values. The fitting procedure is constrained by the physical form of the IS and TD components, which limits parameter correlations and reduces fitting ambiguity. The IS component is most sensitive to noise and initial guesses due to its low intensity, whereas the $TD_{fast}$ and $TD_{slow}$ components are more robustly determined. Consequently, the extracted branching fractions are primarily governed by the TD components and are less sensitive to fitting uncertainties.

In the VA experiments presented here, two TD components are identified and thus two independent $I_{TDa}$ and $I_{TDb}$ functions and convolutions must be constructed and further convoluted with the beam and IS components. Finally, a non-linear least squares fitting procedure uses numerical minimization to optimize the free fitting parameters. By comparing the fitting quality of one TD component fitting and two TD component fitting as shown in Fig. S1 in the SI, it is obvious that one TD component is insufficient to describe the desorption profiles. Confidence intervals presented in the results include propagated errors from the measurement and analysis procedure. Systematic errors, which dominate the displayed uncertainties,

may arise from the QMS detection and beam intensity fluctuations during measurements. Non-systematic errors from unstable environmental chamber conditions during experiments are difficult to estimate, however, the experimental procedure is designed to minimize them.

The temperature dependence of the desorption rate coefficient can be extracted from the fitting procedure assuming Arrhenius type behavior,

$$k = Ae^{\left(-\frac{E_a}{k_B T_s}\right)}, \quad (4)$$

where $A$ is a pre-exponential factor and $E_a$ is the activation energy for thermal desorption. Thus, if observed desorption rates extracted from the ToF distributions follow Arrhenius type behavior the activation energy, can be calculated from a linear least squares fitting of the data plotted as $\ln k$ *versus* $1/T$, as illustrated by rearranging eqn (4),

$$\ln k = -\frac{E_a 1}{k_B T} + \ln A. \quad (5)$$

The angular flux for molecules leaving the substrate surface may generally be described by a $\cos(\theta - \theta_{max})^n$ distribution, where $\theta_{max}$ is the peak scattering angle with respect to the surface normal direction, $\theta$ is the observation angle also with respect to the surface normal, and $n$ is a shape factor which either narrows or broadens the flux. Thermalized molecules lose their initial momentum in interactions with the surface and consequently desorb in all directions with no preference related to their incident direction. Thus, for the TD component, $\theta_{max} = 0$ and $n = 1$, resulting in a typical $\cos(\theta)$ desorption distribution. This makes it easy to estimate the TD probability by observing the flux at any single scattering angle. The total integrated TD intensity $I_{TD}^{VA}$ is used to assess the absolute probability of thermal desorption of water molecules from the surface $P_{TD}$. The $P_{TD}$ for $D_2O$ on a VA is retrieved by comparing $I_{TD}^{VA}$ with desorption from a clean graphite surface $I_{TD}^{G}$ under similar conditions,

$$P_{TD} = \frac{S_G I_{TD}^{VA}}{I_{TD}^{G}}, \quad (6)$$

and using a sticking coefficient for water on graphite $S_G = 0.73 \pm 0.07$.[38]

The total integrated intensity for inelastic scattering $I_{IS}^{VA}$ of water molecules from a VA surface is more difficult to estimate as it has a directed flow related to the MB incident angle. Thus $I_{IS}^{VA}$ is quantified by assuming that scattering out of the plane, relative to the incident beam, has a similar angular profile as the in-plane scattering. A $\cos(\theta - \theta_{max})^n$ function with $\theta_{max} = 49$–$53^\circ$ and $n = 26$–$69$ describes a narrow IS flux with a maximum close to the specular angle. The absolute inelastic scattering probability $P_{IS}$ is obtained by normalizing $I_{IS}^{VA}$ to $P_{TD}$. Molecules that are thermalized in the interaction with the surface and stay there for times longer than the experimental measurement time (10 ms) are assumed to be sticking on the surface. Thus a sticking coefficient $\alpha$ may be calculated from the absolute trapping desorption and inelastic scattering probabilities,

$$\alpha = 1 - P_{TD} - P_{IS}. \quad (7)$$

### 2.3. Molecular dynamics simulations

Complementary MD simulations have been performed to characterize water interactions with solid VA surfaces between 200 and 240 K. A standard OPLS-AA force field[45] is used for VA with implementation of RESP charges fitted on an electric field induced by Kohn–Sham orbitals calculated with BLYP-D3/DZVP *ab initio* data.[41] The equations of motion are integrated using the leap-frog algorithm[46] as part of the GROMACS package.[47] All bonds are constrained with the LINCS algorithm enabling the use of a 2 fs time step.[48] A cut off distance of 0.85 nm is applied for the short-range interactions, and long-range electrostatic interactions are treated using the Particle Mesh Ewald method.[49] Temperature is held at the desired value using the V-rescale algorithm with a coupling time of 0.1 ps.[50]

The VA crystal lattice is modeled based on the structure characterized with X-ray diffraction.[51] The crystal super cell is created by duplicating the unit cell in the $x$, $y$ and $z$ directions. After geometrical optimization, which removed all spurious contacts, the crystal is equilibrated in a NPT ensemble for 10 ns. In the next step, the slab surface is created by cutting the crystal in a given direction. Two alternative VA surfaces are chosen and energies are calculated to find a slab with the most energetically favorable surface, here determined to be a surface separating two monolayers. The simulation system consists of 4 352 atoms placed in a monoclinic box stretched by vectors sized $15.2 \times 1.9 \times 3.5$ nm and having $\alpha$, $\beta$ and $\gamma$ angles $90^\circ$, $39.59^\circ$ and $90^\circ$ respectively. The simulation box is extended 2 nm in the $x$ direction (perpendicular to the surface) on each side to avoid image interactions between the slabs.

The VA crystal is gradually heated from 210 K to 270 K by performing simulated annealing in the NVT ensemble over 160 ns, and a simulated melting point is determined, $T_m = 255$ K. Subsequently, water interactions with the VA surface are investigated over a temperature range from $0.78T_m$ to $0.95T_m$ with simulations designed to resemble experimental conditions. Water is modeled with the SPC/E model[52] where the choice of potential is motivated by previous work on carbohydrate interactions with water.[53] Single water molecules are propagated towards the surface at a $45^\circ$ angle with respect to the surface normal direction and an incident kinetic energy equal to $22.5 \pm 0.5$ kJ mol$^{-1}$ (corresponding to a velocity of 1626 ms$^{-1}$). Thenitial positions of water molecules are randomly chosen at a distance of 1 nm from the surface, and 5000 trajectories are propagated for 60 ps at each studied surface temperature. The water molecules are decoupled from the thermostat to avoid influencing the collision dynamics. The MD simulations are thus performed for single-water molecules under low-coverage, dry conditions and over short timescales, and therefore do not capture finite water coverage effects or the

long-timescale desorption processes observed in the EMB experiments.

# 3. Results

## 3.1. Results from EMB experiments

In Fig. 2a–c ToF distributions for water intensity as a function of time are presented. The time dependent flux is shown for a solid VA layer at 160 K (Fig. 2a), and for a molecularly thin VA layer on graphite at 260 K (Fig. 2b and c). The flux from the surface is either measured in the surface normal direction (Fig. 2a and b), or at an observation angle $\theta = 60^\circ$. In the figure a complete non-linear convolution fitting is also presented, in addition to deconvoluted individual components. The measured time dependent flux is mathematically modeled by convoluting the functions that describe inelastic scattering eqn (1), fast and slow desorption (independent uses of eqn (2) and (3)), and the incident beam (Fig. 2d). Thus, the velocity profile of the incident molecular beam (Fig. 2d), measured by rotating the QMS directly into the path of the beam, is an important aspect when determining the history of the measured molecules. The distance between the beam source, surface and detector results in a beam position within the ToF window equal to that of hypothetical elastic scattering from the surface. Deviations from the hypothetical elastic scenario are due to energy transfer during surface contact. Inelastic scattering is observed in the initial part of the surface scattered flux for observation angles corresponding to forward scattering (Fig. 2c). The TD observations are well captured when the desorbing component is split into two components, $TD_{fast}$ and $TD_{slow}$, as illustrated in Fig. 2 including the inset in Fig. 2a that displays the results on a logarithmic scale. This behavior indicates that the majority of molecules undergo trapping followed by rapid desorption, with a smaller fraction accessing longer-lived surface states. These observations are further discussed in Section 4 in terms of trapping and desorption mechanisms.

Inelastically scattered molecules typically lose 50–80% of their incident kinetic energy when colliding with the studied VA surfaces (Fig. 3). Within the experimental uncertainty, no clear trend is observed in the retained kinetic energy as a function of scattering angle. This is consistent with molecules that transfer energy efficiently both along and perpendicular to the surface plane, suggesting that water molecules interact with a relatively rough VA surface. The majority of the water molecules trap and thermalize on the studied VA surfaces, and reside there for some time ($\tau$) before desorbing with a behavior that may be described with a temperature-dependent desorption rate coefficient ($k$). The water desorption observed from the VA surface is composed of two desorption components with distinct desorption rates. For $TD_{fast}$ the desorption rate is too fast to be experimentally resolved ($\tau_{fast} \leq 10$ μs), while for $TD_{slow}$ $\tau_{slow} \approx 0.5$–2.5 ms. The temperature-dependent desorption rate coefficient for the slow process is plotted in an Arrhenius fashion in Fig. 4. An activation energy for desorption and a pre-exponential factor are derived from the

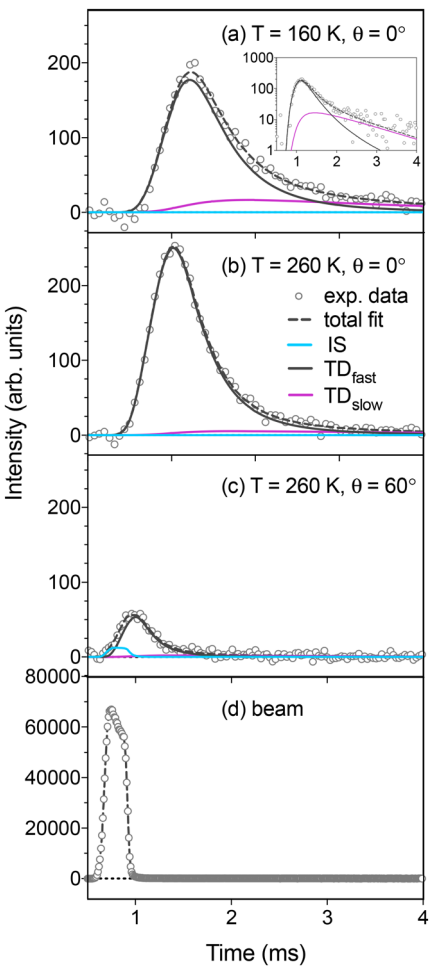


Fig. 2 Experimental ToF distributions of water intensities in the flux from (a) a solid micrometer thick VA layer at 160 K for observation angle 0°, and (b) a molecularly thin coating of VA on graphite at 260 K for observation angles 0° and (c) 60°, as well as (d) the incident molecular beam profile. Superimposed are the nonlinear least-squares fits of the data with IS (blue line), fast TD (black line) and slow TD (pink line) components, and the full fit (black dashed line). The inset in panel (a) shows experimental data and fits on a logarithmic scale. The experimental data have been smoothened by a 30 μs centered moving average.

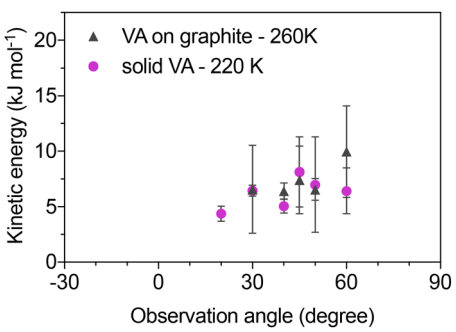


Fig. 3 The kinetic energy of inelastically scattered molecules as a function of observation angle in EMB experiments from a solid VA layer (pink dots) and a molecularly thin VA coating on graphite (black triangles). The maximum value on the y-scale represents the incident MB intensity (22.5 ± 0.5 kJ $mol^{-1}$).

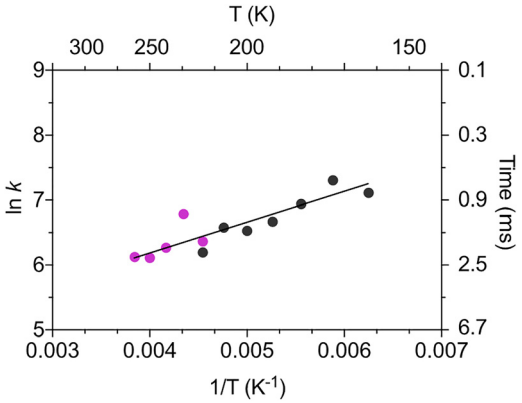


Fig. 4 Arrhenius plot, showing the natural logarithm of the slow desorption rate coefficient as a function of $1/T$. The line represents a linear regression to the experimental data points, with $E_a = -3.8$ kJ mol$^{-1}$, $A = 7.8 \times 10^1$ s$^{-1}$. Black dots indicate results from experiments with a solid VA layer and pink dots correspond to results from experiments with a molecularly thin VA coating on graphite.

Arrhenius slope and intercept of the linear regression. The linear regression to the experimental data points in the Arrhenius plot yields $E_{a\_slow} = -3.8$ kJ mol$^{-1}$ and $A_{slow} = 7.8 \times 10^1$ s$^{-1}$. The low $A$ and the negative $E_a$ value indicate that the path to water desorption is a complex process involving more than one reaction step and the results do not provide direct information of a surface binding energy. The Arrhenius fit should therefore be regarded as an empirical description of the apparent $TD_{slow}$ kinetics rather than evidence for a single elementary desorption process. The derived $E_a$ and $A$ values are effective parameters reflecting a complex, multi-step process and should not be interpreted as direct adsorption energetics. This suggests that the slow desorption channel reflects a complex, multi-step process rather than a single elementary desorption event. The implications of this behavior for the underlying desorption mechanism are discussed in Section 4.

The impinging water molecules that are observed to remain on the surface for the entire experimental measurement time (10 ms), are defined as undergoing sticking on the surface. The sticking probability $\alpha$ eqn (7) on molecularly thin VA coatings on graphite and thick solid layers at different temperatures is presented in Fig. 5, together with the $TD_{fast}$ and $TD_{slow}$ fractions. The results are dominated (69–83%) by fast TD at all temperatures, with a minor contribution (7–16%) from slow TD, and no clear temperature dependence is observed. The same is true for the sticking probability $\alpha$, that exhibits little variation with temperature. However, there is a small difference in $\alpha$ between thin VA coatings and thick solid VA layers, where more water is trapped on a thin layer ($0.15 \leq \alpha \leq 0.20$) than on a thick layer ($0.05 \leq \alpha \leq 0.15$). This phenomenon is contrary to observations reported in a recent study of the water/nopinone system.[35] As described in Section 3.2, the VA molecules form dimers positioned horizontally along the multilayer surfaces, however, for the monolayer it seems that the carboxylic groups are more readily available on the surface, *i.e.* the dimer structure does not form or it is less stable compared to the bulk structure. The weak temperature dependence of $\alpha$ indicates that the structure of the molecularly thin VA layer does not undergo major changes in the investigated temperature range. This indicates that film thickness, rather than temperature, plays a more important role in determining water uptake under these conditions. This difference between thin and thick VA layers is discussed further in Section 4.

A lower limit for the activation energy of molecules undergoing sticking may be calculated from the experimental data and conditions. Assuming Arrhenius behavior at the maximum experimental temperature, a minimum surface residence time of 10 ms and a typical pre-exponential factor of $10^{13}$ s$^{-1}$ for ordinary desorption,[54] the activation energy for molecules undergoing sticking is estimated to be $\geq 55$ kJ mol$^{-1}$, representing a lower-bound value based on assumed Arrhenius behavior, a characteristic residence time, and a typical pre-exponential factor, rather than a direct measurement.

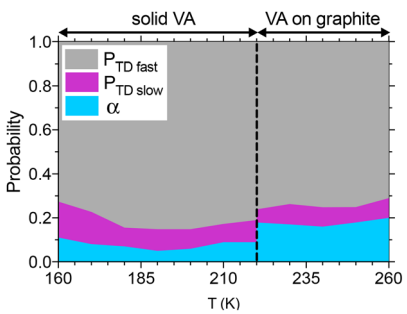


Fig. 5 Experimental sticking probabilities ($\alpha$) of water on VA surfaces (blue area) and the fractions undergoing slow TD (pink area) and fast TD (gray area) as a function of temperature. Results for $T \leq 220$ represents solid VA, and results for $T \geq 220$ K corresponds to experiments with a thin VA coating on graphite. The IS probability is not shown, which is about $2 \pm 1\%$, and it is insensitive to layer thickness or temperature.

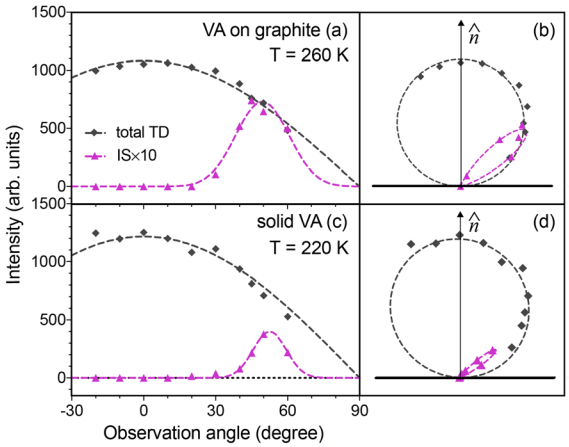


Fig. 6 Angular distributions of integrated experimental IS $\times$ 10 (pink triangles and dashed line) and TD (black dots and dashed line) components from a VA (a) and (b) coating on graphite at 260 K, and (c) and (d) a micrometer thick solid VA layer at 220 K. $\hat{n}$ and arrow represent the surface normal direction.

The angular dependencies of the IS and TD components are calculated by integrating each component at all observation angles. In Fig. 6 angular distributions and polar plots that result from water interactions with a molecularly thin VA coating on graphite at 260 K and a thick solid VA layer at 220 K (Fig. 6a–d, respectively) are displayed. The inelastic components are minor parts of the total fluxes and their values are multiplied by a factor of ten to make them more visible. Inelastic scattering occurs predominantly in the forward direction with the peak of the distributions shifted slightly below the specular direction. Conversely, molecules that are thermalized in contact with the surface lose their incident momentum and desorb in random directions. The resulting TD profiles are typical cosine distributions relative to the surface normal, as expected for ordinary thermal desorption.

### 3.2. Results from MD simulations

Molecular dynamics simulations provide complementary information about the molecular-level water–VA interactions. The VA crystal structure consisting of zig-zagging VA dimers results in the appearance of functional groups on the surface. This is illustrated in Fig. 7a, which displays the oxygen density on the surface at a temperature of $0.78T_m$. Fig. 7b shows the tilt angle distribution of VA molecules in the uppermost surface layer at three temperatures spanning $T_m$. The tilt angle is defined as the angle between the surface normal direction and the VA chain direction, and thus indicates the orientation of VA molecules. At low temperatures surface molecules have a uniform direction, which is an indication of an organized structure. As temperature increases, surface molecules tend to lose their common organization, and this tendency results in a significantly broader distribution at $1.1T_m$, indicating reduced orientational order while still retaining a preference for lower tilt angles.

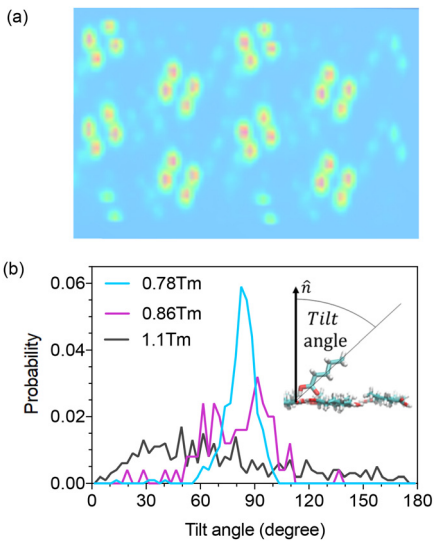


Fig. 7 (a) Projection of oxygen density on the VA surface at $0.78T_m$, where red and blue colors represent high and low probability respectively. (b) Tilt angle distributions of VA molecules in the topmost surface layer at temperatures $1.1T_m$ (black line), $0.86T_m$ (pink line) and $0.78T_m$ (blue line). The tilt angle is defined as the angle between the surface normal and the VA chain direction.

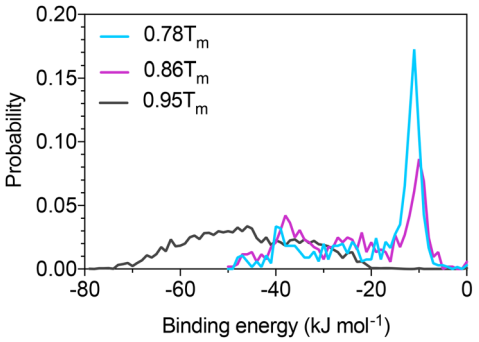


Fig. 8 Binding energy distributions from MD simulations for adsorbed molecules after $t$ = 60 ps, for three different temperatures relative to the melting point ($T_m$): $0.78T_m$ (blue line), $0.86T_m$ (pink line) and $0.95T_m$ (black line).

Most of the incoming water molecules are thermalized (see Fig. S2 in SI) and a fraction of them subsequently desorb from the surface. From the MD simulations we can directly see $TD_{fast}$ and IS. Molecules that undergo IS preserve ~50% of their initial KE (*e.g.*, 9 kJ mol$^{-1}$ at 20° and 11 kJ mol$^{-1}$ at 75° scattering angle, compared to the incident KE ≈ 22.5 kJ mol$^{-1}$). In addition, binding energy distributions of the remaining fraction of water molecules on the VA surface hint at the existence of $TD_{slow}$. Fig. 8 shows binding energy distributions experienced by adsorbed water monomers on VA for three different temperatures. At low temperatures the majority of molecules remain on the VA surface at the end of the 60 ps simulation run and are only weakly bound (−10 kJ mol$^{-1}$), but with a fraction being able to find more strongly bound sites that could result in sticking on longer time scales. As temperature increases the probability of finding strongly bound molecules also increases, with a substantial change as the melting temperature is approached. This supports the presence of both weakly and more strongly bound states contributing to the observed desorption behavior. These findings are discussed in Section 4 in relation to the experimental desorption behavior.

Fig. 9 illustrates some of the typical adsorption scenarios of water molecules on VA surfaces. At low temperatures configurations with a water molecule adsorbed on top of the VA dimer dominate, and yield binding energies of ~10 kJ mol$^{-1}$ (Fig. 9a). However, some molecules become incorporated into the uppermost monolayer with binding energy of ~40 kJ mol$^{-1}$ (Fig. 9b). When the temperature is increased and approaches the melting point configurations with higher binding energies are favored (Fig. 9c).

## 4. Discussion

The results presented above reveal several key features of the water–VA interaction, which are discussed below. The collection of results from EMB experiments and MD simulations

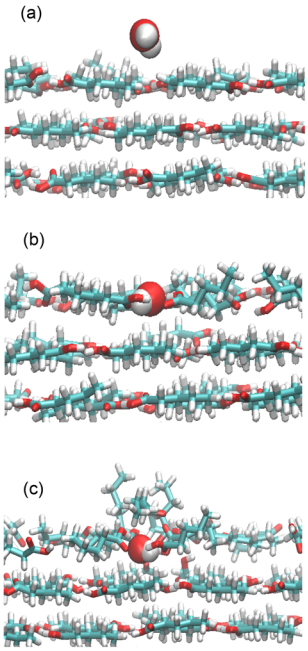


Fig. 9 MD simulation snapshots of water molecules bound with binding energies equal to (a) ~10 kJ mol$^{-1}$, (b) ~40 kJ mol$^{-1}$ and (c) ~50 kJ mol$^{-1}$. The VA slab is kept at (a) 0.78$T_m$, (b) 0.86$T_m$ and (c) 0.95$T_m$.

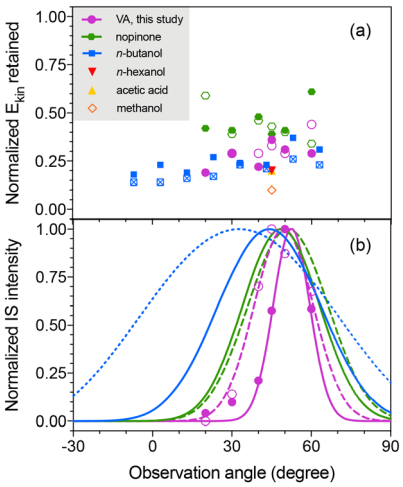


Fig. 10 Experimental data from this and previous studies. Normalized (a) retained kinetic energy and (b) intensity distributions of inelastically scattered water molecules as a function of angle for VA (pink dots), nopinone (green hexagons),[35] *n*-butanol (blue squares),[34] *n*-hexanol (red triangle),[31] acetic acid (yellow triangle)[32] and methanol (red diamond)[37] systems. Filled symbols and solid lines represent micrometer thick solid organic surfaces, and open symbols and dashed lines represent thin organic coatings on graphite. A liquid *n*-butanol surface is represented by crossed squares and a dotted line.

presented here are in general agreement. The majority of impinging water molecules interact weakly with the VA surface layer and a major fraction is experimentally observed to leave the surface by fast desorption. A similar behavior has been observed for other organic surfaces.[32,34,35] These weakly bound molecules correspond to the simulated molecules that desorb on picosecond timescales. Such weakly bound molecules are free to diffuse on the surface and eventually desorb. Surface diffusion is relatively fast and molecules have a substantial chance to penetrate the uppermost VA layer and find surface sites with relatively high binding energies. However, especially at lower temperatures the VA dimers coupled by the carboxyl groups leave the functional groups less accessible for water to form hydrogen bonds. From strong binding sites water molecules may either be released to desorb ($TD_{slow}$), or find more strongly bound states where they remain (stick) on the 10 ms time scale of the experiments. This complex desorption pattern with more than one TD component has been observed in previous EMB studies of water interacting with *n*-butanol surfaces.[34]

The observed collision dynamics are typical for water interactions with organic surfaces where inelastically scattered molecules tend to lose a significant fraction (50–90%) of their incident kinetic energy in surface contact (Fig. 10a).[29,31–35] Energy transfer between incoming water molecules and surface modes is highly efficient, which results in trapping probabilities close to unity. Any molecules that are nevertheless able to escape the surface by IS do so with a minor fraction of their initial kinetic energy. The final energy shows limited or no dependence on observation angle, and the results are consistent with efficient energy transfer both parallel and perpendicular to the surface plane. The scattered intensity as a function of angle is also qualitatively comparable for the studied systems (Fig. 10b), with the exception being water interactions with liquid *n*-butanol that results in a significantly wider distribution than observed for the solid surfaces.

Interestingly, no clear changes in the water trapping-desorption behavior are observed as the temperature of the solid VA layer is increased to 220 K. This is approximately 20 K below $T_m$ and corresponds to 0.92$T_m$, and the results suggest

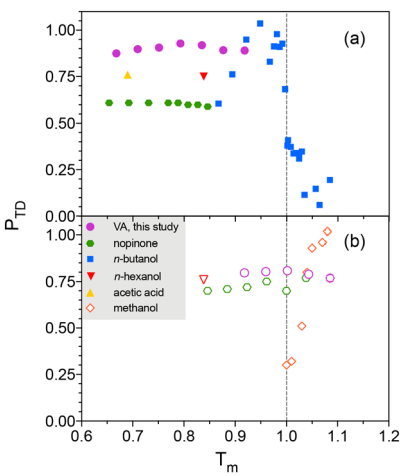


Fig. 11 Experimental data from this and previous studies. Trapping desorption probability from (a) microscopically thick organic layers and (b) thin coatings on graphite of VA (pink dots), nopinone (green hexagons),[35] *n*-butanol (blue squares),[34] *n*-hexanol (red triangles),[31] acetic acid (yellow triangles)[32] and methanol (red diamonds, as a function of temperature relative to the bulk melting point ($T_m$).[37]

that changes in surface properties do not play a major role for the desorption probability at this temperature. For comparison, Fig. 11 summarizes the observed trapping-desorption probability as function of temperature for several systems recently studied by the EMB method. The VA results are similar to data for other organic surfaces, with the exception being *n*-butanol where changes in surface structure influence water uptake well below the melting point (Fig. 11a). Similar conclusions can be drawn for molecularly thin layers of organic compounds on graphite (Fig. 11b), where methanol is the exception that displays a clear temperature dependence. Note that the melting point for these thin layers may deviate significantly from the bulk $T_m$ indicated on Fig. 11.

The negative temperature dependence of the desorption rate constants (Fig. 4) observed for $TD_{slow}$ is intriguing. Generally, molecules that are trapped in a weakly bound state desorb with a higher rate as temperature is increased. Absent changes in surface structure with increasing temperature, this increased desorption will allow molecules less time to diffuse to sites with higher binding energies. However, it is unlikely that over a significant temperature range a surface layer will remain unaffected by an increasing temperature. Instead changes in surface structure and breaking hydrogen bonds within the VA surface layer can be expected to provide increased opportunities for forming strong surface bonds with water molecules. This is illustrated by the MD simulations as the temperature approaches the melting point (Fig. 9). Adding complexity to the situation is the fact that the MD simulations are carried out under ''dry'' conditions with single water molecules interacting with the VA surface. The MD simulations are thus performed for single-water molecules under low-coverage, dry conditions and over short timescales (60 ps), and therefore do not capture finite water coverage effects or the long-timescale desorption processes observed in the EMB experiments. Conversely, in the EMB experiments, a low but finite surface coverage of water may build up and provide additional opportunities for water–water interactions and the formation of relatively strong hydrogen bonds. These competing processes may affect the experimentally observed temperature dependence.

This study illustrates the complexity of molecular-level processes at the interface between gas and condensed organic phases. An interesting detail is the observed differences between solid organics and thin coatings. In particular graphite with its smooth surface character appears to have a significant impact on the properties and behavior of adsorbates. The stability of the thin organic coatings is significantly higher than the micrometer thick layers, which indicates that they are structurally different. EMB experiments show that trapping desorption probabilities for water on thin methanol coatings have a clear temperature dependence with decreasing desorption as one goes from high to low temperatures and $T_m$ is approached (Fig. 11b).[29] Such trends are absent for water desorbing from thin coatings of nopinone[35] and VA. However, the melting temperatures of thin coatings are likely to deviate from those of the bulk, as is the case for methanol coatings that have a substantially lower melting temperature (135 K) compared to the bulk (175.4 K).[29] The weak temperature dependence of the $P_{TD}$ for thin VA and nopinone coatings (Fig. 11b) may signify that the thin layer melting points differ significantly from the bulk $T_m$.

The observed difference in sticking probability on thin coatings compared to thick adsorbed layers also indicates a difference in surface properties. This has previously been seen for organics such as *n*-hexanol,[31] acetic acid[32] and nopinone.[35] However, the observed higher uptake on thin VA coatings relative to micrometer thick layers is opposite to the trend seen in the previously mentioned studies.[31,32,35] Further studies will be required to elucidate the underlying structural and dynamic differences responsible for the observed trends.

## 5. Conclusions

In this study, EMB measurements and MD simulations were combined in molecular-level investigations of water interactions with VA surfaces. Water impinging onto VA surfaces is observed to undergo efficient trapping. A major fraction desorbs rapidly, while a minor fraction is able to find more strongly bound surface states. The more strongly bound molecules may subsequently desorb on millisecond time scales, or stick for longer time periods. Molecular dynamics simulations reveal that water molecules are able to find sites within the uppermost surface layer. As the temperature is increased and approaches the melting point, bonds between carboxyl functional groups can be broken, allowing water molecules to become fully incorporated into the surface layer. As the temperature approaches the melting point, intermolecular hydrogen bonding and packing interactions between VA molecules become partially disrupted, leading to increased surface disorder and molecular mobility. This can expose functional groups and allow water molecules to penetrate into and become incorporated within the uppermost surface layer.

The surface state of the condensed layers is of central importance for the water uptake processes. The results obtained from these EMB experiments and MD simulations are not indicative of VA surface melting at temperatures up to $0.92T_m$. This is an important finding because in the atmospheric context surface state highly influences mass transfer, surface chemistry, and other physicochemical properties of aerosol particles.

The observed water sticking coefficients are also observed to have only weak temperature dependencies in the investigated range. However, we do observe a discontinuity between the uptake on molecularly thin VA layers on graphite *versus* thicker VA layers. This suggests that the thin VA coating on graphite may have a different molecular arrangement compared to micrometer thick layers that may contribute to a higher possibility for water accommodation.

The employed EMB and MD methods contribute to the molecular-level understanding of organic systems of atmospheric importance. The investigated surfaces are proxies for the organic mixtures that can be expected to be found under

atmospheric conditions, and further studies of increasingly complex systems are needed to build a modelling framework for atmospheric applications.

## Author contributions

Sofia M. Johansson: investigation (EMB), data curation, formal analysis, writing – original draft. Josip Lovrić: investigation (MD), methodology, data curation. Erik S. Thomson: writing – review & editing. Xiangrui Kong: conceptualization, supervision, writing – review & editing. Jan B. C. Pettersson: conceptualization, supervision, funding acquisition, writing – review & editing.

## Conflicts of interest

There are no conflicts to declare.

## Data availability

All data supporting the findings of this study are available within the article and its supplementary information (SI). Additional data related to this work are available from the corresponding author upon reasonable request. Supplementary information is available. See DOI: https://doi.org/10.1039/d6cp01088a.

## Acknowledgements

The authors acknowledge funding from the Swedish Research Council (2021-04042, 2020-03497), the Carl Tryggers Stiftelse for Scientific Research (CTS 23:2526, CTS 24:3137).

## References

1 R. J. Charlson, S. E. Schwartz, J. M. Hales, R. D. Cess, J. A. Coakley, J. E. Hansen and D. J. Hofmann, *Science*, 1992, **255**, 423–430.
2 J. Li, B. E. Carlson, Y. L. Yung, D. Lv, J. Hansen, J. E. Penner, H. Liao, V. Ramaswamy, R. A. Kahn, P. Zhang, O. Dubovik, A. Ding, A. A. Lacis, L. Zhang and Y. Dong, *Nat. Rev. Earth Environ.*, 2022, **3**, 363–379.
3 J. L. Jimenez, M. R. Canagaratna, N. M. Donahue, A. S. H. Prevot, Q. Zhang, J. H. Kroll, P. F. DeCarlo, J. D. Allan, H. Coe, N. L. Ng, A. C. Aiken, K. S. Docherty, I. M. Ulbrich, A. P. Grieshop, A. L. Robinson, J. Duplissy, J. D. Smith, K. R. Wilson, V. A. Lanz, C. Hueglin, Y. L. Sun, J. Tian, A. Laaksonen, T. Raatikainen, J. Rautiainen, P. Vaattovaara, M. Ehn, M. Kulmala, J. M. Tomlinson, D. R. Collins, M. J. Cubison, J. Dunlea, J. A. Huffman, T. B. Onasch, M. R. Alfarra, P. I. Williams, K. Bower, Y. Kondo, J. Schneider, F. Drewnick, S. Borrmann, S. Weimer, K. Demerjian, D. Salcedo, L. Cottrell, R. Griffin, A. Takami, T. Miyoshi, S. Hatakeyama, A. Shimono, J. Y. Sun, Y. M. Zhang, K. Dzepina, J. R. Kimmel, D. Sueper, J. T. Jayne, S. C. Herndon, A. M. Trimborn, L. R. Williams, E. C. Wood, A. M. Middlebrook, C. E. Kolb, U. Baltensperger and D. R. Worsnop, *Science*, 2009, **326**, 1525–1529.
4 W. Li, A. Ito, G. Wang, M. Zhi, L. Xu, Q. Yuan, J. Zhang, L. Liu, F. Wu, A. Laskin, D. Zhang, X. Zhang, T. Zhu, J. Chen, N. Mihalopoulos, A. Bougiatioti, M. Kanakidou, G. Wang, H. Hu, Y. Zhao and Z. Shi, *Natl. Sci. Rev.*, 2025, **12**, nwaf221.
5 IPCC, Climate change 2013: The physical science basis. Contribution of working group I to the fifth assessment report of the Intergovernmental Panel on Climate Change, Cambridge University Press, Cambridge, United Kingdom and New York, NY, USA, 2013.
6 Y. Sun, H. Luo, Y. Li, W. Zhou, W. Xu, P. Fu and D. Zhao, *npj Clim. Atmos. Sci.*, 2025, **8**, 305.
7 A. Chebbi and P. Carlier, *Atmos. Environ.*, 1996, **30**, 4233–4249.
8 S. Gagan, K. Sarang, K. J. Rudzinski, R. Liu, R. Szmigielski and Y. Zhang, *Atmos. Environ.*, 2023, **312**, 120017.
9 M. D. Petters and S. M. Kreidenweis, *Atmos. Chem. Phys.*, 2007, **7**, 1961–1971.
10 M. Shiraiwa and U. Pöschl, *Atmos. Chem. Phys.*, 2021, **21**, 1565–1580.
11 C. R. Ruehl, J. F. Davies and K. R. Wilson, *Science*, 2016, **351**, 1447–1450.
12 G. Wang, R. Zhang, M. E. Gomez, L. Yang, M. Levy Zamora, M. Hu, Y. Lin, J. Peng, S. Guo, J. Meng, J. Li, C. Cheng, T. Hu, Y. Ren, Y. Wang, J. Gao, J. Cao, Z. An, W. Zhou, G. Li, J. Wang, P. Tian, W. Marrero-Ortiz, J. Secrest, Z. Du, J. Zheng, D. Shang, L. Zeng, M. Shao, W. Wang, Y. Huang, Y. Wang, Y. Zhu, Y. Li, J. Hu, B. Pan, L. Cai, Y. Cheng, Y. Ji, F. Zhang, D. Rosenfeld, P. S. Liss, R. A. Duce, C. E. Kolb and M. J. Molina, *Proc. Natl. Acad. Sci. U. S. A.*, 2016, **113**, 13630–13635.
13 F. Xie, Y. Su, Y. Tian, Y. Shi, X. Zhou, P. Wang, R. Yu, W. Wang, J. He, J. Xin and C. Lü, *Atmos. Chem. Phys.*, 2023, **23**, 2365–2378.
14 J. P. Reid, A. K. Bertram, D. O. Topping, A. Laskin, S. T. Martin, M. D. Petters, F. D. Pope and G. Rovelli, *Nat. Commun.*, 2018, **9**, 956.
15 Z. Zhang, Y. Li, H. Ran, J. An, Y. Qu, W. Zhou, W. Xu, W. Hu, H. Xie, Z. Wang, Y. Sun and M. Shiraiwa, *Atmos. Chem. Phys.*, 2024, **24**, 4809–4826.
16 T. Koop, J. Bookhold, M. Shiraiwa and U. Pöschl, *Phys. Chem. Chem. Phys.*, 2011, **13**, 19238–19255.
17 M. Darvas, S. Picaud and P. Jedlovszky, *Phys. Chem. Chem. Phys.*, 2013, **15**, 10942–10951.
18 D. Vardanega and S. Picaud, *J. Chem. Phys.*, 2014, **141**, 104701.
19 B. Radola, S. Picaud, D. Vardanega and P. Jedlovszky, *J. Phys. Chem. B*, 2015, **119**, 15662–15674.
20 A. Roose, C. Toubin, S. Dusanter, V. Riffault and D. Duflot, *ACS Earth Space Chem.*, 2019, **3**, 380–389.
21 C. Zhang, Z. Zhang, L. Bu, Y. Yang, W. Xiong and Y. Wang, *Particuology*, 2023, **77**, 128–135.
22 C. Zhang, Z. Zhang, W. Xiong, Y. Yang and Y. Wang, *Atmos. Environ.*, 2024, **319**, 120305.

 

23 M. Lbadaoui-Darvas, S. Takahama and A. Nenes, *Atmos. Chem. Phys.*, 2021, **21**, 17687–17714.
24 A. D. Bond, *New J. Chem.*, 2004, **28**, 104–114.
25 B. Hendrik, D. F. Ogletree, S. F. Charles, H. Zahid and S. Miquel, *J. Phys.: Condens. Matter*, 2002, **14**, L227.
26 X. Kong, D. Castarède, A. Boucly, L. Artiglia, M. Ammann, T. Bartels-Rausch, E. S. Thomson and J. B. C. Pettersson, *J. Phys. Chem. C*, 2020, **124**, 5263–5269.
27 S. M. Johansson, X. Kong, P. Papagiannakopoulos, E. S. Thomson and J. B. Pettersson, *Rev. Sci. Instrum.*, 2017, **88**, 035112.
28 X. Kong, P. U. Andersson, N. Markovic and J. B. C. Pettersson, in *Physics and Chemistry of Ice 2010*, ed. Y. Furukawa, G. Sazaki, T. Uchida and N. Watanabe, Hokkaido University Press, Sapporo, 2011, pp. 79–88.
29 E. S. Thomson, X. R. Kong, P. U. Andersson, N. Markovic and J. B. C. Pettersson, *J. Phys. Chem. Lett.*, 2011, **2**, 2174–2178.
30 P. Papagiannakopoulos, X. R. Kong, E. S. Thomson, N. Markovic and J. B. C. Pettersson, *J. Phys. Chem. C*, 2013, **117**, 6678–6685.
31 X. R. Kong, E. S. Thomson, P. Papagiannakopoulos, S. M. Johansson and J. B. C. Pettersson, *J. Phys. Chem. B*, 2014, **118**, 13378–13386.
32 P. Papagiannakopoulos, X. R. Kong, E. S. Thomson and J. B. C. Pettersson, *J. Phys. Chem. B*, 2014, **118**, 13333–13340.
33 S. M. Johansson, X. Kong, E. S. Thomson, M. Hallquist and J. B. C. Pettersson, *J. Phys. Chem. A*, 2017, **121**, 6614–6619.
34 S. M. Johansson, J. Lovric, X. Kong, E. S. Thomson, P. Papagiannakopoulos, S. Briquez, C. Toubin and J. B. C. Pettersson, *Phys. Chem. Chem. Phys.*, 2019, **21**, 1141–1151.
35 S. M. Johansson, J. Lovric, X. Kong, E. S. Thomson and J. B. C. Pettersson, *J. Phys. Chem. A*, 2020, **124**, 3652–3661.
36 X. Kong, P. Papagiannakopoulos, E. S. Thomson, N. Markovic and J. B. Pettersson, *J. Phys. Chem. A*, 2014, **118**, 3973–3979.
37 E. S. Thomson, X. Kong, N. Marković, P. Papagiannakopoulos and J. B. C. Pettersson, *Atmos. Chem. Phys.*, 2013, **13**, 2223–2233.
38 N. Markovic, P. U. Andersson, M. B. Nagard and J. B. C. Pettersson, *Chem. Phys.*, 1999, **247**, 413–430.
39 X. Kong, E. S. Thomson, N. Markovic and J. B. C. Pettersson, *ChemPhysChem*, 2019, **20**, 2171–2178.
40 X. Kong, J. Lovrić, S. M. Johansson, N. L. Prisle and J. B. C. Pettersson, *J. Phys. Chem. A*, 2021, **125**, 6263–6272.
41 X. Kong, Y. Lian, S. Jiang and J. Pettersson, *EGUsphere*, 2026, preprint, https://doi.org/10.5194/egusphere-2026-525.
42 X. Kong, C. Toubin, A. Habartova, E. Pluharova, M. Roeselova and J. B. C. Pettersson, *J. Phys. Chem. A*, 2018, **122**, 4861–4868.
43 W. M. Haynes, *Physical Constants of Organic Compounds in CRC Handbook of Chemistry and Physics*, CRC Press, Taylor & Francis Group, Boca Raton, FL, 2014.
44 C. R. Arumainayagam and R. J. Madix, *Prog. Surf. Sci.*, 1991, **38**, 1–102.
45 W. L. Jorgensen, D. S. Maxwell and J. Tirado-Rives, *J. Am. Chem. Soc.*, 1996, **118**, 11225–11236.
46 L. Verlet, *Phys. Rev.*, 1967, **159**, 98–103.
47 D. Van Der Spoel, E. Lindahl, B. Hess, G. Groenhof, A. E. Mark and H. J. C. Berendsen, *J. Comput. Chem.*, 2005, **26**, 1701–1718.
48 B. Hess, H. Bekker, H. J. C. Berendsen and J. G. E. M. Fraaije, *J. Comput. Chem.*, 1997, **18**, 1463–1472.
49 U. Essmann, L. Perera, M. L. Berkowitz, T. Darden, H. Lee and L. G. Pedersen, *J. Chem. Phys.*, 1995, **103**, 8577–8593.
50 G. Bussi, D. Donadio and M. Parrinello, *J. Chem. Phys.*, 2007, **126**, 014101.
51 R. L. Sass and R. F. Scheuerman, *Acta Crystallogr.*, 1962, **15**, 77–81.
52 H. J. C. Berendsen, J. R. Grigera and T. P. Straatsma, *J. Phys. Chem.*, 1987, **91**, 6269–6271.
53 J. Lovric, D. Duflot, M. Monnerville, C. Toubin and S. Briquez, *J. Phys. Chem. A*, 2016, **120**, 10141–10149.
54 V. N. Kontratev, *Chemical Kinetics of Gas Reactions*, Pergamon Press, London, England, 1964.